Since January 2020 Elsevier has created a COVID-19 resource centre with free information in English and Mandarin on the novel coronavirus COVID-19. The COVID-19 resource centre is hosted on Elsevier Connect, the company's public news and information website.

Journal of Environmental Chemical Engineering 10 (2022) 108697

Contents lists available at ScienceDirect

Journal of Environmental Chemical Engineering

journal homepage: www.elsevier.com/locate/jece

Atomically dispersed Mn boosting photoelectrochemical SARS-CoV-2 spike protein immunosensing on carbon nitride

Yunfan Jia [a], Yun Chen [a], Li Xu [a], Junchao Qian [b], Feng Chen [b], Yakun Wan [c], Henan Li [a,*], Huaming Li [a,*]

[a] Key Laboratory for Theory and Technology of Intelligent Agricultural Machinery and Equipment, School of Chemistry and Chemical Engineering, Institute for Energy Research, Jiangsu University, Zhenjiang 212013, China
[b] Jiangsu Key Laboratory for Environment Functional Materials, Jiangsu Key Laboratory of Intelligent Building Energy Efficiency, Suzhou University of Science and Technology, Suzhou 215009, China
[c] Shanghai Novamab Biopharmaceuticals Co., Ltd., Shanghai 201318, China

ARTICLE INFO

Editor: Dr. G. Palmisano

Keywords:
COVID-19
Spike protein
Photoelectrochemical immunosensor
Nanobody
Carbon nitride

ABSTRACT

The sudden outbreak of coronavirus disease (COVID-19) triggered by SARS-CoV-2 infection has created a terrifying situation around the world. The spike protein of SARS-CoV-2 can act as an early biomarker for COVID-19. Therefore, controlling the spread of COVID-19 requires a low-cost, fast-response, and sensitive monitoring technique of spike protein. Herein, a photoelectrochemical (PEC) immunosensor for the detection of spike protein was constructed using the nanobody and an Mn (II) modified graphitic carbon nitride (Mn/g-C_3N_4). The introduction of atomically dispersed Mn (II) can accelerate the effective transfer and separation of photo-generated electron-hole pairs, which significantly boosts PEC performance of g-C_3N_4, thereby improving the detection sensitivity. As a recognition site, nanobody can achieve high-affinity binding to the spike protein, leading to a high sensitivity. The linear detection range of the proposed PEC immunosensor was 75 fg mL^{-1} to 150 pg mL^{-1}, and the limit of detection was calculated to be 1.22 fg mL^{-1}. This stable and feasible PEC immunosensor would be a promising diagnostic tool for sensitively detecting spike protein of SARS-CoV-2.

1. Introduction

The global outspread of coronavirus disease 2019 (COVID-19) has dramatically posted serious damage to public health [1,2]. With its fast-spreading speed and high mortality rate, severe acute respiratory syndrome coronavirus 2 (SARS-CoV-2) is considered to be the main driver of infection [3]. Currently, the SARS-CoV-2 detection methods are mainly divided into two categories: molecular detection of nucleic acid and immunological detection of antigen and antibody. As a method of molecular detection, reverse transcription polymerase chain reaction (RT-PCR) is the gold standard for detection and identification. However, the high detection requirements, high cost, and complexity of RT-PCR limit its widespread use in underdeveloped countries [4]. The immunoassay method provides initial screening for the presence of corresponding antigen present in COVID-19 patients, which allows timely testing at a low cost [5]. Immunoassay is an efficient, sensitive, and convenient method for determining the content of analytes through specific recognition between antigen and antibody [6,7]. As a reverse transcriptase virus, the SARS-CoV-2 virus has four main proteins: spike (S) protein, membrane (M) protein, envelope (E) protein, and nucleocapsid (N) protein [8,9]. Among them, S protein can be used as a main antigen biomarker to diagnose COVID-19 [10,11]. In general, the selection of the recognition element in immunoassays is also critical. The use of S protein-derived peptides, antibodies, and amino-aptamers as recognition elements to detect the S protein of SARS-CoV-2 has been reported [12–14].

Nanobody (Nb) is a variable domain fragment derived from the heavy-chain-only antibody in camels [15]. As the smallest antibody fragment discovered, Nb has opened the way toward diagnosis and treatment due to the merits of great thermal stability, orderly immobilization, and high affinity [16]. Furthermore, Nb can easily recognize cryptic epitopes compared with conventional full-size antibodies due to its small size [17]. For example, Nb is orientedly immobilized to the surface of microcantilevers and specifically binds to a carcinoembryonic antigen, thereby realizing the highly selective detection of tumor markers [16]. Thus, Nb can be employed to design a sensitive

* Corresponding authors.
E-mail addresses: lhn@ujs.edu.cn (H. Li), lihm@ujs.edu.cn (H. Li).

https://doi.org/10.1016/j.jece.2022.108697
Received 7 July 2022; Received in revised form 29 September 2022; Accepted 30 September 2022
Available online 3 October 2022

immunosensor as a specific recognition element. PEC sensing approach is an innovative detection method with the advantages of low background current, high sensitivity and fast detection speed, which is used in environmental pollutants, food safety and medical fields [18,19]. The label-free PEC immunosensor combines the intrinsic sensitivity of the PEC method and the peculiarity of specific binding with immune molecules, which can quickly and simply detect biological molecules [20]. When the antigen and antibody are combined, a steric hindrance effect is created in the detection platform of PEC immunosensor. The reduction of photocurrent can function as a signal output, which realizes the detection of the antigen.

Making photoactive materials with outstanding photoelectric conversion efficiency is one of the keys to improving the detection sensitivity of PEC immunosensors [21,22]. Graphitic carbon nitride (g-C_3N_4) materials have sparked great interest in the construction of PEC sensors owing to their adjustable electronic and optical absorption properties, simple synthesis method, and biocompatibility [23,24]. While pristine g-C_3N_4 has some weaknesses such as rapid recombination of carriers and low electrons transfer ability, leading to poor PEC performance [23,25]. Some modification strategies such as the construction of heterojunction [26,27], grafting molecular or functional groups [28], and introduction of the metal element [29] have been implemented to boost PEC performance of pristine g-C_3N_4. The introduction of metal element can accelerate the transmission of electron-hole pairs, boost the effective separation and enhance the visible light-harvesting, thus resulting in excellent PEC performance [30,31]. The introduction of Cu (I) has been reported to improve the visible light utilization and broaden the absorption wavelength of g-C_3N_4, and the constructed Cu (I)/g-C_3N_4-based PEC aptasensor has realized highly sensitive determination of bisphenol A [32]. Modifying single atom into the semiconductor can effectively improve its charge transport behavior and restrict the recombination of photoinduced carriers, thereby significantly enhancing PEC performance [33,34]. Mn has been well studied in ion modification because of many kinds of oxidation states, and the materials modified by Mn ions have high conductivity and charge transfer ability [35]. Thus, the development of g-C_3N_4 photoactive materials with atomic Mn (II) modified can provide a possibility to construct a high-sensitivity PEC immunosensing platform.

In this work, a highly sensitive label-free PEC immunosensor based on Mn (II) modified g-C_3N_4 (Mn/g-C_3N_4) was fabricated to detect SARS-CoV-2 S protein (Scheme 1). After introducing atomically dispersed Mn (II) into g-C_3N_4, the PEC performance can be improved by increasing the photoelectric conversion efficiency, thereby endowing the immunosensor with high sensitivity. The specific recognized Nb was effectively immobilized on the Mn/g-C_3N_4electrode, enabling highly selective detection of S protein. Additionally, the PEC immunosensor for S protein has the advantages of low cost, excellent stability, and reproducibility.

2. Experimental section

2.1. Chemicals and reagents

Melamine, manganous acetate ($Mn(COOH)_2{\cdot}4H_2O$), KOH, NaOH, HCl, and ethanol were packaged and bought from Sinopharm Chemical Reagent Co., Ltd. (Shanghai, China). The above chemicals were used without the purification process. Phosphate buffered solution (PBS, 6.7 mM, pH 7.4) and bovine serum albumin (BSA) were purchased from Hyclone Laboratories, USA. Nb and SARS-CoV-2 S protein were obtained from Novamab Biopharmaceuticals Co., Ltd. (Shanghai, China), and the specific screening and extraction procedures are described in this work [36].

2.2. Preparation of Mn/g-C_3N_4

CN was synthesized by a low-temperature calcination method [37]. Melamine (2 g), KOH (0.56 g), and NaOH (0.2 g) were ground in an agate mortar and heated in a muffle furnace at 330 °C for 2 h with a temperature gradient of 5 °C min^{-1}. Then, the calcined sample was washed with 1 M HCl solution and deionized water, and dried under vacuum for 12 h, which was recorded as CN. Subsequently, CN (0.46 g) and $Mn(COOH)_2{\cdot}4H_2O$ (0.12 g) were dissolved into deionized water (60 mL) continuing to stir at 60 °C for 15 h. After that, the resultant mixture was centrifuged under 8,000 rpm for 3 min and dried in a vacuum oven. The final powders were filled in a crucible and calcined in a tube furnace with a rate of 5 °C min^{-1} to 550 °C and maintained for 1 h, where N_2 (80 mL min^{-1}) acts as a protective gas. The annealed

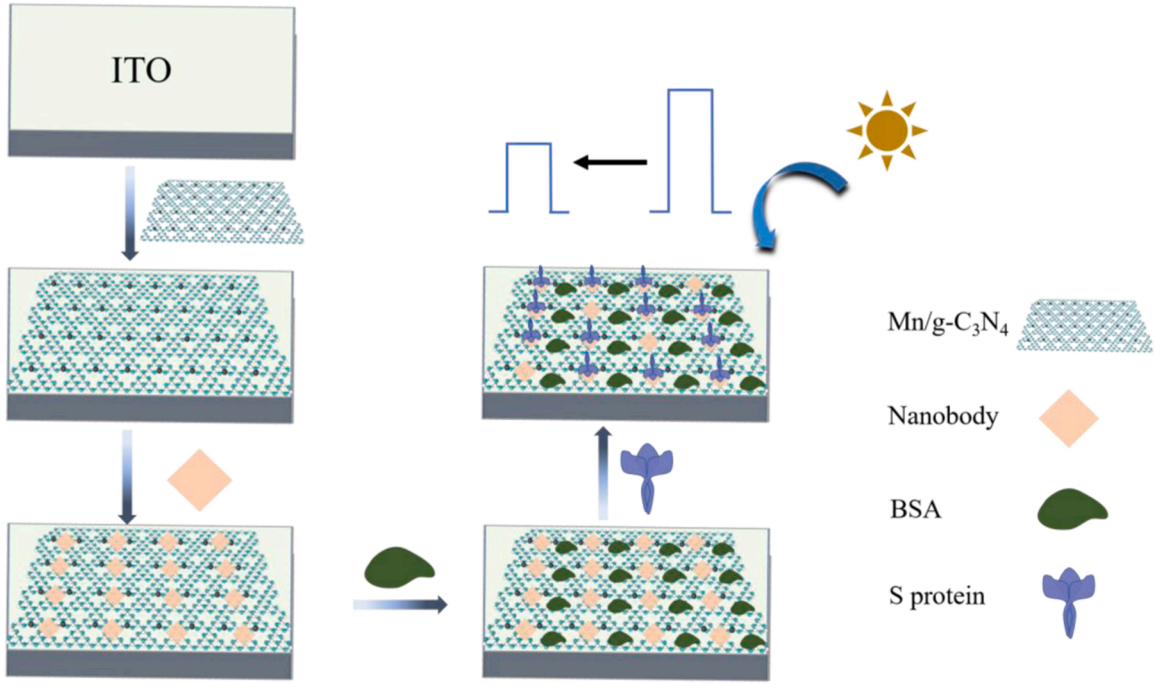

Scheme 1. Schematic illustration of PEC immunosensor using Mn/g-C_3N_4 nanomaterial for detecting SARS-CoV-2 S protein.

sample was dissolved into HCl solution (1 M) and stirred thoroughly, washed with water to neutrality, and then dried under vacuum. After grinding, the final product was denoted as Mn/g-C_3N_4. For comparison, the CN was calcined under the same condition only without the addition of manganese salt and denoted as g-C_3N_4. To obtain materials with optimal PEC performance, composites with different Mn contents were prepared to optimize the loading content of Mn (Fig. S1). The Mn content in the Mn/g-C_3N_4 obtained by the ICP test was 2.33% (Table S1).

2.3. Fabrication of the Mn/g-C_3N_4 based PEC immunosensor

Indium tin oxide (ITO) glass (resistance less than 10 ohm/sq) was supplied from Kaivo Optoelectronic Technology (Zhuhai, China). Before modification, ITO was pretreated by ultrasonically washing with deionized water and ethanol. The homogeneously dispersed Mn/g-C_3N_4 suspension (1 mg mL^{-1}, 50 μL) obtained by the ultrasonic method was added dropwise to the conductive surface of ITO electrodes with a determined area of 0.5 cm^2, which were remarked as Mn/g-C_3N_4/ITO after drying. Subsequently, Nb (0.406 μg mL^{-1}, 10 μL) was incubated on the Mn/g-C_3N_4/ITO electrode at room temperature for 12 h, then flushed with PBS to remove excess Nb. The resulting electrode was labeled as Nb/Mn/g-C_3N_4/ITO. Next, BSA (5 wt%, 10 μL) was added dropwise to the Nb/Mn/g-C_3N_4/ITO electrode and kept for 30 min at room temperature. Then the electrode was rinsed several times with PBS and dried, named BSA/Nb/Mn/g-C_3N_4/ITO. Finally, different concentrations of S protein (10 μL) were dropped onto the BSA/Nb/Mn/g-C_3N_4/ITO electrode for incubation of 30 min by rinsing with PBS. Then the obtained SP/BSA/Nb/Mn/g-C_3N_4/ITO electrode for subsequent PEC testing.

2.4. PEC measurements

Photocurrent and electrochemical impedance spectroscopy (EIS) experiments were tested on the CHI660E electrochemical workstation (CH Instruments Ins., Shanghai, China). The photocurrent response was performed in PBS by a conventional three-electrode system with a xenon lamp (PLS-FX300HU, Beijing Perfectlight, China) as the light source. In addition, EIS measurements were carried out at a frequency of 0.1–100 kHz and without light irradiation. Impedance solution was prepared by uniformly mixing equimolar solutions of phosphate buffer (0.1 M, pH 7.0), $[Fe(CN)_6]^{3-/4-}$ (5 mM), and KCl (0.1 M). Phosphate buffer was obtained by mixing 0.1 mol L^{-1} Na_2HPO_4 and 0.1 mol L^{-1} NaH_2PO_4 to adjust pH 7.0. Mott-Schottky curves (~1.0 kHz, CH Instrument) was performed by 0.5 mol L^{-1} Na_2SO_4 solution under dark condition. All the photocurrent measurements were operated at a potential of 0 V.

3. Results and discussion

3.1. Structural and morphology characterization of materials

Fig. 1**a** shows the XRD pattern of g-C_3N_4 with two peaks at 27.3° and 13.1°, corresponding to (002) plane of layer-to-layer stacking state with conjugated aromatic systems and (100) plane of triazine within the layers [38]. The similar diffraction peaks of Mn/g-C_3N_4 and g-C_3N_4 indicate that the structure of g-C_3N_4 is unaffected by the low content intercalation of Mn. Furthermore, there are not any diffraction peaks shown for Mn/g-C_3N_4, which indicates that common compounds such as MnO_2 and Mn_2O_3 are inexistent. The structures of g-C_3N_4 are unaffected by the introduction of various Mn contents (Fig. S2). FT-IR spectra (Fig. 1**b**) show that g-C_3N_4 and Mn/g-C_3N_4 display some characteristic peaks situated at 810 cm^{-1} and 1200 ~ 1700 cm^{-1}, mainly attributed to the respiratory vibration of the tri-s-triazine ring and the tensile vibration of C–NH_X and C═N [39]. Additionally, there is a sharp band located at 2177 cm^{-1} rooted from stretching vibrations of ≡C≡N, which is mainly the result of hydroxide melts treatment [39]. This phenomenon is attributed to the loss of the terminal amino group of carbon nitride caused by the addition of molten salt. Likewise, the introduction of Mn does not significantly change the position of peak vibration, and Mn/g-C_3N_4 still maintains the intrinsic skeleton of g-C_3N_4. As shown in Fig. S3, Raman spectra of the samples were measured at the excitation wavelength of 532 nm. Both g-C_3N_4 and Mn/g-C_3N_4 exhibit strong Raman signals with comparable peak positions. The presence of the characteristic peak associated with Mn is also not observed in

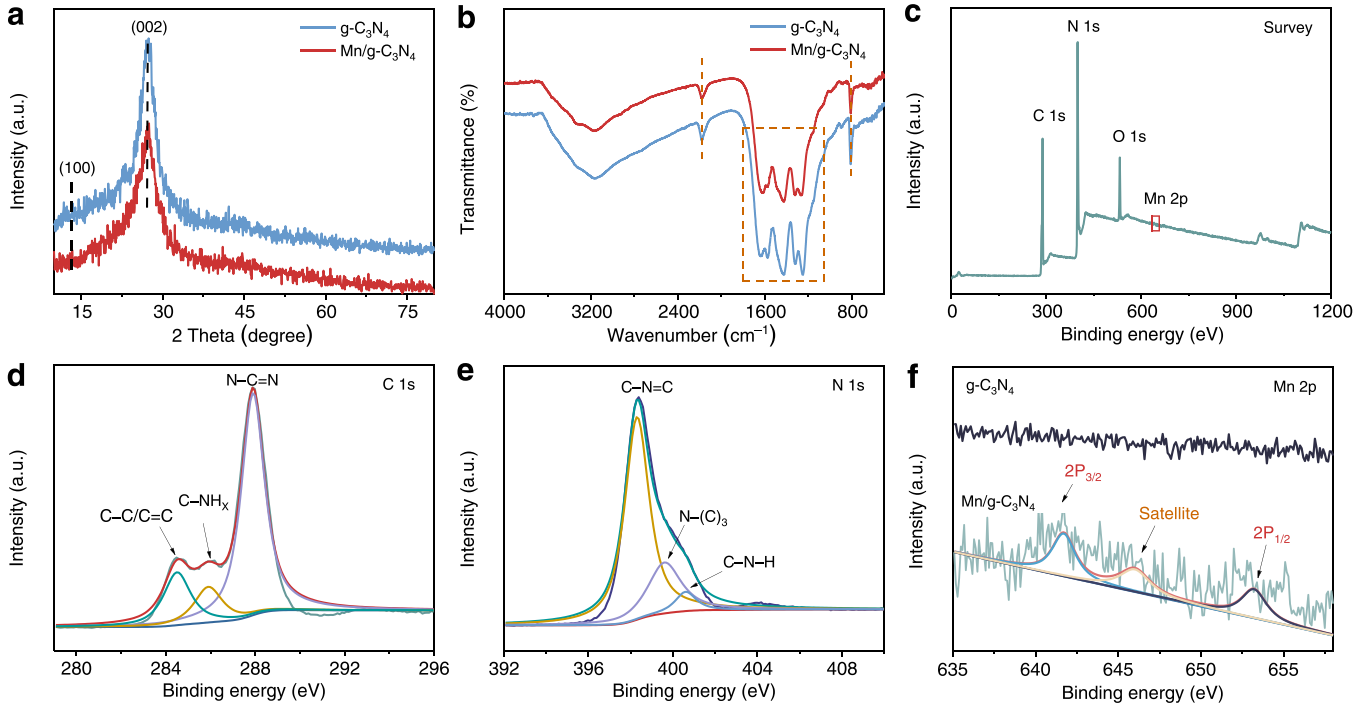

Fig. 1. XRD patterns (a), FT-IR spectra (b), and Mn 2p XPS spectra (f) of g-C_3N_4 and Mn/g-C_3N_4; XPS spectra of Mn/g-C_3N_4: (c) Survey, (d) C 1 s and (e) N 1 s.

Mn/g-C_3N_4. This indicates that the presence of Mn does not change the framework structure of carbon nitride, which is consistent with the FT-IR results.

The XPS survey of Mn/g-C_3N_4 has four main elements (Fig. 1**c**): C, N, O, and Mn, indicating that Mn was successfully doped into g-C_3N_4. More concretely, two peaks at 284.5 and 288.0 eV correspond to C–C/C═C and N–C═N species in the C1s spectrum (Fig. 1**d**) [40]. The observed peak at 286.0 eV is attributed to the carbon connected to the amino group (C–NH_x) and C═N [38], which echoes the result of the FT-IR spectra. As demonstrated in Fig. 1**e**, the peaks centered at 398.3, 399.6, and 400.6 eV of the N 1 s spectrum are derived from sp^2 hybrid aromatic C═N–C, pyrrole nitrogen N–$(C)_3$, and quaternary nitrogen C–NH, respectively [41,42]. The O 1 s spectrum (Fig. S4) contains only a single peak of adsorbed oxygen at 531.8 eV [32], which can also confirm that there is no Mn–O bond, and Mn does not exist in the form of oxides. As illustrated in Fig. 1**f**, the Mn 2p spectrum of g-C_3N_4 only shows a noise line without any characteristic peak. And the Mn 2p spectrum is decomposed into three main peaks at 641.7, 653.2, and 646.0 eV, which are assigned to Mn $2p_{3/2}$, Mn $2p_{1/2}$ signals, and satellite peaks, respectively. The information revealed by the Mn 2p XPS spectrum indicates that the valence state of Mn is identified as positive divalent [43,44]. The above XPS results confirm that Mn/g-C_3N_4 was successfully synthesized.

The overall morphology of the samples was analyzed by SEM and TEM. As shown in Fig. 2**a**, **c,** and S5, Mn/g-C_3N_4 and g-C_3N_4 display similar porous layered nanosheet structures. The dispersion state of Mn (II) in the Mn/g-C_3N_4 was further identified with the aberration-corrected HAADF-STEM (Fig. 2**b**) [45]. The isolated bright spots belong to the presence of atomically dispersed Mn sites, implying that Mn (II) as a single atom is mainly dispersed on the g-C_3N_4 substrate [46]. The bright spots marked by red circles are Mn because Mn atoms have a higher atomic number and are heavier than C and N atoms. In addition, the corresponding EDS mapping images (Fig. 2**d**) demonstrate the presence of C, N, O, and Mn elements, and the specific element content is shown in Fig. S6. Therefore, the analysis results of XPS and HAADF-STEM images further demonstrate that atomically dispersing Mn (II) species successfully modified into g-C_3N_4.

The Brunauer–Emmett–Teller (BET) method and Barrett–Joyner–Halenda (BJH) analysis of g-C_3N_4 and Mn/g-C_3N_4 samples were performed to measure the surface area and pore-size distribution, respectively. Fig. 2**e** shows the N_2 adsorption desorption isotherms, and the consequences exhibit that g-C_3N_4 and Mn/g-C_3N_4 are typical IV isotherms, which indicates the presence of mesoporous structure [47]. The specific surface areas of g-C_3N_4 and Mn/g-C_3N_4 are respectively determined as 16.78 m^2 g^{-1} and 22.73 m^2 g^{-1}. Moreover, abundant pores can be observed in Fig. 2**f**. Compared with g-C_3N_4, the pore size of Mn/g-C_3N_4 increases, which is consistent with the results of TEM images.

3.2. Optical and PEC performance

The photoabsorption capability of g-C_3N_4 and Mn/g-C_3N_4 was performed by UV–vis absorption spectra (200–800 nm). As depicted in Fig. 3**a**, by comparing the spectra of g-C_3N_4 and Mn/g-C_3N_4, Mn/g-C_3N_4 presents an excellent light-harvesting capability. The maximum absorption edge of Mn/g-C_3N_4 occurs in a slight red shift of ~20 nm compared to g-C_3N_4, indicating that the introduction of Mn (II) increases the light utilization, generating amounts of electrons and holes. The introduced Mn forms impurity energy levels in g-C_3N_4, which narrows the forbidden band width of the doped samples, and the photogenerated electron-hole pairs are easier to excite, which can improve the light capture and electron transfer capability, thus endowing the material with excellent PEC performance [48]. The related M-S plots, Tauc plots, and schematic band structure of g-C_3N_4 and Mn/g-C_3N_4 are shown in

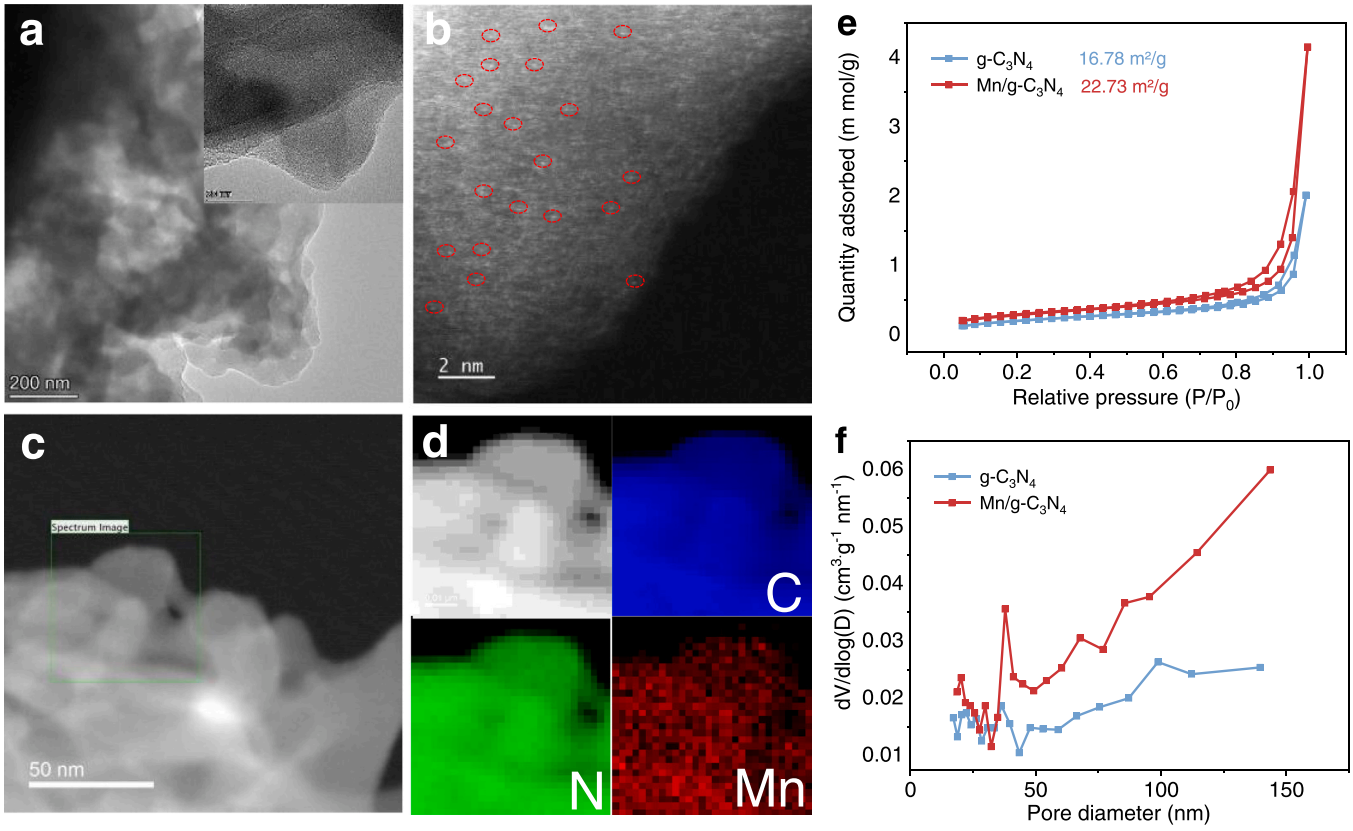

Fig. 2. TEM (a, insert: HRTEM image), HAADF-STEM (b, atomically dispersed Mn is highlighted), and HRTEM (c) images of Mn/g-C_3N_4; EDS mapping (d) of Mn/g-C_3N_4: C (blue), N (green), and Mn (red); N_2 adsorption and desorption isotherms (e) and the corresponding pore-size distribution (f) of g-C_3N_4 and Mn/g-C_3N_4.

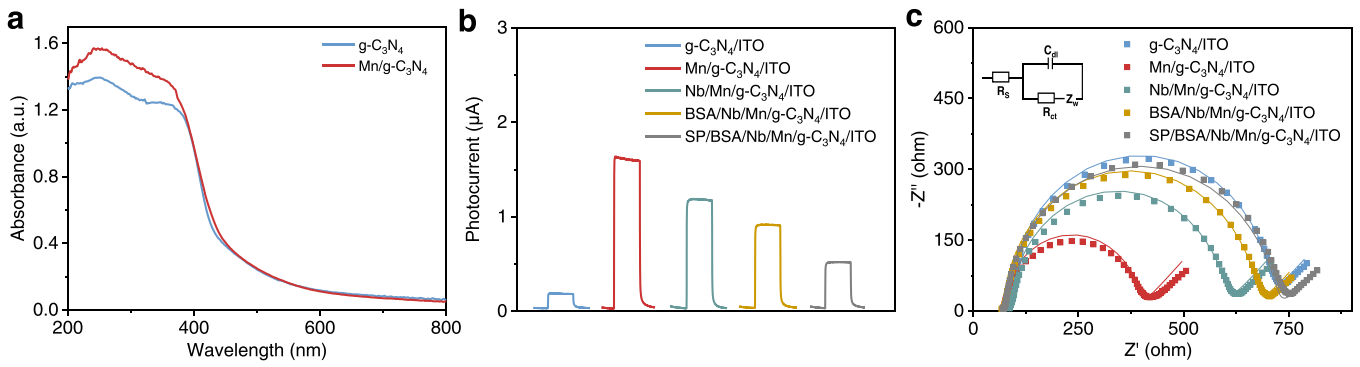

Fig. 3. (a) UV–vis absorption spectra of g-C_3N_4 and Mn/g-C_3N_4; Photocurrent response (b) and EIS curves (c) of the prepared electrodes (dot and line represent the measured data and calculated results).

Fig. S7.

Chronoamperometric i-t curve and EIS can effectively reveal the conversion and separation of photoinduced carriers. Transient photocurrent of g-C_3N_4 and Mn/g-C_3N_4 was recorded at a 20 s interval of light off-on without the applied potential. g-C_3N_4 exhibits a lower photocurrent signal than Mn/g-C_3N_4 owing to the efficient recombination of photoinduced carriers (Fig. 3**b**). The photocurrent value of Mn/g-C_3N_4 was 10 times larger compared with g-C_3N_4, confirming that the modification of Mn (II) can stimulate the separation of photoinduced charges, thereby enhancing the photocurrent response [49]. EIS spectra represent the charge transfer ability of g-C_3N_4 and Mn/g-C_3N_4. The semicircle demonstrates a smaller radius, and the relative material has a faster charge transfer speed [50]. The semicircle of Mn/g-C_3N_4/ITO is the smallest, signifying that Mn (II) enhances the charge transfer capability. The equivalent circuit model was calculated using ZSimpWin software to further verify the EIS results (Fig. 3**c**). C_{dl}, R_s, R_{ct}, and Z_w in the inset mean interfacial capacitance, solution resistance, charge transfer resistance, and Warburg impedance in solution, respectively (Table S2). The actual measured (dot) is well matched with the calculated (line) data, which shows that the fitting circuit diagram is reasonable. After the introduction of Mn (II), the R_{ct} value of Mn/g-C_3N_4/ITO (~318.9 Ω) was less than that of g-C_3N_4/ITO (~639 Ω). The above results show that Mn/g-C_3N_4 with excellent PEC performance can provide powerful evidence for the construction of PEC immunoassay platform.

3.3. PEC immunoassay platform

Based on Mn/g-C_3N_4 as a photoelectrically active material with superior PEC performance, it is possible to fabricate a label-free PEC immunosensor for sensitively detecting S protein. The specific design process is shown in Fig. 4**a**. The detection mechanism of the proposed PEC immunosensor is based on the hindrance effect between the Nb and S protein, which inhibits the separation and transfer of carriers, resulting in the reduction of photocurrent signal. There is a π-π stacking

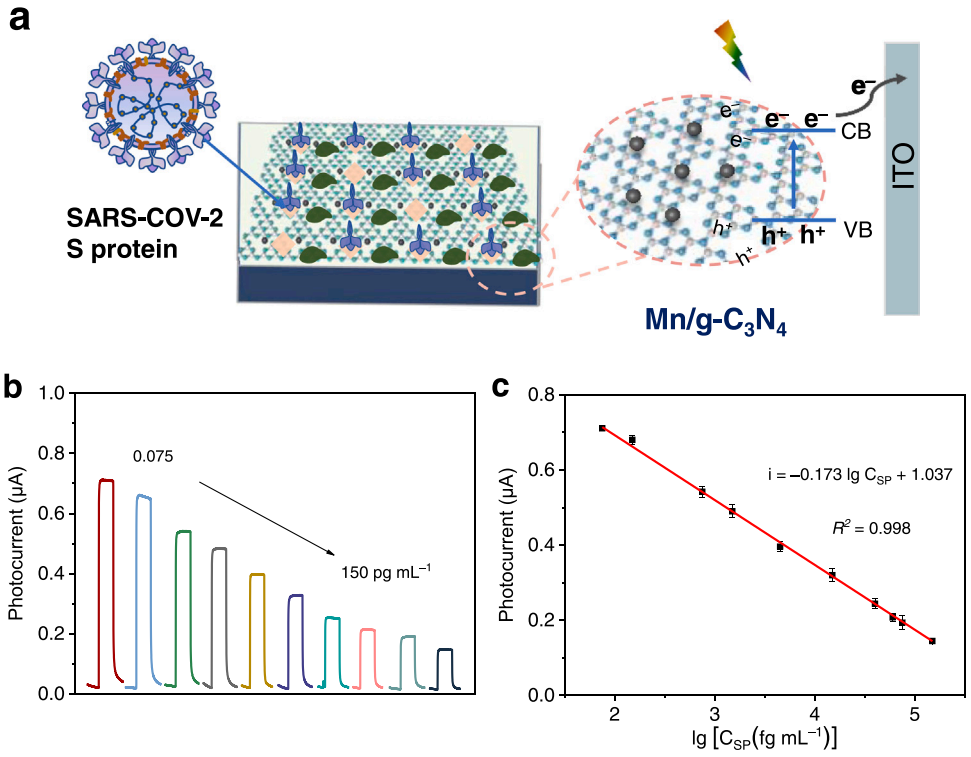

Fig. 4. (a) Schematic diagram of photoinduced electron transfer of Mn/g-C_3N_4 in the immunosensor; (b) Photocurrent of PEC immunosensor based on BSA/Nb/Mn/g-C_3N_4/ITO electrode with various concentrations of S protein: 0.075, 0.15, 0.75, 1.5, 4.5, 15, 40, 60, 75, 150 pg mL^{-1}; (c) Linear plot. Data were obtained by three parallel measurements.

interaction with the conjugated heptazine structural unit of g-C_3N_4, which promotes Nb to be stably anchored to the Mn/g-C_3N_4 electrode without any modification [51]. Fig. 3**b** shows the photocurrent response of Mn/g-C_3N_4/ITO, Nb/Mn/g-C_3N_4/ITO, BSA/Nb/Mn/g-C_3N_4/ITO, and SP/BSA/Nb/Mn/g-C_3N_4/ITO electrode. After Nb was incubated on the surface of the Mn/g-C_3N_4/ITO electrode, the photocurrent signal gradually decreased. Because the addition of Nb biomolecules hinders the steric effect and inhibits the electrons transfer [18]. Similarly, the effect of adding BSA is that the non-specific recognition sites of Nb and g-C_3N_4 are blocked [52]. When S protein at a concentration of 1.5 pg mL^{-1} was immersed into BSA/Nb/Mn/g-C_3N_4/ITO electrode, the S protein and the Nb underwent a specific immunoreaction, inhibiting the transfer of electrons and resulting in a reduced photocurrent. Meanwhile, the construction process of the immunosensor was further assessed by EIS measurement. With the addition of Nb and BSA, the R_{ct} gradually increased (503.5 Ω; 595.3 Ω), indicating that each component successfully modified on the electrode surface to inhibit the photoinduced electron migration. After the electrode was incubated with S protein, the impedance of SP/BSA/Nb/Mn/g-C_3N_4/ITO electrode further increased to an R_{ct} value of 610.6 Ω. This is because the modified insulating protein on the electrode surface creates a steric hindrance to block electrons transfer, thereby increasing the R_{ct} value. According to the above results, Mn/g-C_3N_4-based PEC immunosensor for quantitative sensitive detection of S protein was successfully constructed.

The constructed PEC immunosensor was optimized with the concentration of Nb (0.406 μg mL^{-1}, Fig. S8). As illustrated in Fig. 4**b**, the concentrations of S protein increased from 0.075 to 150 pg mL^{-1}, and the photocurrent response shows a gradual decline. The possible reason is that when the concentration of S protein increases, Nb specifically binds to S protein to strike the immunoreaction, and then many immunocomplexes are enriched on the electrode surface, which reduces the photocurrent response. When the concentration continued to increase (300, 750, 1,500, 4,500, 7,500, 10,500, 15,000 pg mL^{-1}), the photocurrent tended to be saturated (Fig. S9). Therefore, the linear detection range was 75 fg mL^{-1} to 150 pg mL^{-1}, and the upper limit of the concentration of the nonlinear deviation of this sensor was 15,000 pg mL^{-1}. From Fig. 4**c**, the measured photocurrent value exhibited a linearly decreasing trend with the logarithmic increase of S protein concentration. The linear equation was I (μA) = –0.173 log[C_{SP} (fg mL^{-1})]+ 1.037 with a obtained correlation coefficient (R^2) of 0.998. Moreover, the detection limit was calculated by the least-squares equation of a calibration curve to be 1.22 fg mL^{-1}. Compared with some reported methods of detecting SARS-CoV-2 (Table S3), this label-free PEC immunosensor has achieved high-sensitivity detection of S protein.

The anti-interference characteristics of the immunosensor were studied by the target S protein and substances that can coexist with saliva samples, such as ascorbic acid, L-glutamic acid, ciprofloxacin, and their mixtures. As shown in Fig. 5**a**, the selected interfering substance can cause no significant effect on the photocurrent signal of PEC immunosensor. Based on the specific experiments reported in the literature [36], it is further demonstrated that Nb can specifically and selectively bind to the RBD mutants in S protein of SARS-CoV-2. Fig. 5**b** shows the short-term stability of SP/BSA/Nb/Mn/g-C_3N_4 electrodes. After the light on-off irradiation test at a 20 s interval, there is no significant change trend in the observed photocurrent signal. To evaluate the long-term storage stability of the immunosensor, the BSA/Nb/Mn/g-C_3N_4 electrodes incubated with S protein were stored in the dark at 4 °C (Fig. 5**c**). After the SP/BSA/Nb/Mn/g-C_3N_4 electrode was stored for 21 days, its photocurrent had no obvious attenuation, demonstrating good stability of the immunosensor platform. Fig. 5**d** displays the photocurrent on different BSA/Nb/Mn/g-C_3N_4/ITO electrodes with the immersed 1.5 pg mL^{-1} S protein by the same modification method. SP/BSA/Nb/Mn/g-C_3N_4 electrode shows a similar photocurrent response with smaller error values (RSD of 1.47%), indicating the good reproducibility of this designed PEC immunosensor. The standard addition concentration of S protein in PBS can be calculated via the linear equation of the sensor to assess the feasibility of PEC immunosensor. Recovery was varying from 96.9% to 101.6%, and the RSD value was 1.68–3.50% as displayed in Table S4. The results indicate that

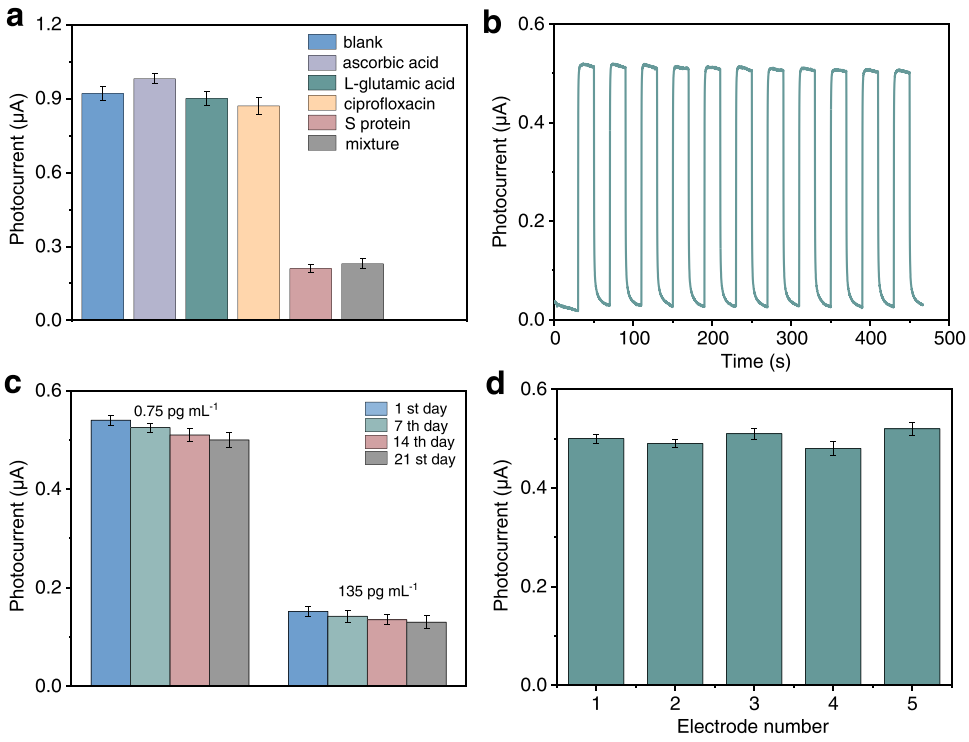

Fig. 5. (a) Selectivity of PEC immunosensor with 60 pg mL^{-1} S protein and 6 ng mL^{-1} different interference substances; (b) Short-term stability with 1.5 pg mL^{-1} S protein. (c) Long-term storage stability for the immunosensing incubated 0.75 and 135 pg mL^{-1} S protein; (d) Repeatability test of the PEC immunosensor with 1.5 pg mL^{-1} S protein. Error bars are equal to SD (n = 3).

the proposed PEC immunosensor provides a sensitive platform for quantitatively detecting SARS-CoV-2 S protein.

4. Conclusions

In summary, a label-free PEC immunosensor using Mn/g-C_3N_4 as the active material and Nb as the specific recognition substrate was successfully fabricated for the sensitive detection of SARS-CoV-2 S protein. The introduction of atomically dispersed Mn (II) enhances the capability of light capture, accelerates separation and transmission efficiency of photoinduced charges, and improves photocurrent response. The Mn/g-C_3N_4 with superior PEC performance was used to construct PEC immunosensor for detecting S protein. The introduction of Nb with high binding capacity can improve the selectivity of the immunosensor for S protein. Therefore, this immunosensor exhibited a wide linear range (75 fg mL^{-1} to 150 pg mL^{-1}), good sensitivity, selectivity, and stability. This work proposes a novel approach for the construction of high-performance PEC immunosensors and also provides a new method for sensitive monitoring of the COVID-19 virus.

CRediT authorship contribution statement

Yunfan Jia: Conceptualization, Formal analysis, Writing – original draft. **Yun Chen:** Investigation, Validation. **Li Xu:** Supervision, Visualization. **Junchao Qian:** Data analysis. **Feng Chen:** Data analysis. **Yakun Wan:** Conceptualization, Resources. **Henan Li:** Supervision, Writing – review & editing. **Huaming Li:** Supervision.

Declaration of Competing Interest

The authors declare that they have no known competing financial interests or personal relationships that could have appeared to influence the work reported in this paper.

Data Availability

No data was used for the research described in the article.

Acknowledgements

This work has been financially supported by High-tech Research Key Laboratory of Zhenjiang (Grant No. SS2018002), a Project Funded by the Priority Academic Program Development of Jiangsu Higher Education Institutions, Natural Science Foundation of Jiangsu Province (Grant No. BK20180971, BK20180103).

Appendix A. Supporting information

Supplementary data associated with this article can be found in the online version at doi:10.1016/j.jece.2022.108697.

References

[1] Z. Zhang, S. Jiang, X. Wang, T. Dong, Y. Wang, D. Li, X. Gao, Z. Qu, Y. Li, A novel enhanced substrate for label-free detection of SARS-CoV-2 based on surface-enhanced Raman scattering, Sens. Actuators B-Chem. 359 (2022), 131568, https://doi.org/10.1016/j.snb.2022.131568.

[2] Z. Rahmati, M. Roushani, H. Hosseini, H. Choobin, Label-free electrochemical aptasensor for rapid detection of SARS-CoV-2 spike glycoprotein based on the composite of $Cu(OH)_2$ nanorods arrays as a high-performance surface substrate, Bioelectrochemistry 146 (2022), 108106, https://doi.org/10.1016/j.bioelechem.2022.108106.

[3] Z. Rahmati, M. Roushani, H. Hosseini, H. Choobin, An electrochemical immunosensor using SARS-CoV-2 spike protein-nickel hydroxide nanoparticles bioconjugate modified SPCE for ultrasensitive detection of SARS-CoV-2 antibodies, Microchem. J. 170 (2021), 106718, https://doi.org/10.1016/j.microc.2021.106718.

[4] R.M. Zerbinati, M. Palmieri, A.C. Felix, H. Martinho, S. Giannecchini, K.K. To, J.A. L. Lindoso, C.M. Romano,, P.H. Braz-Silva, Use of saliva and RT-PCR screening for SARS-CoV-2 variants of concern: Surveillance and monitoring, J. Med. Virol. 94 (9) (2022) 4518–4521, https://doi.org/10.1002/jmv.27839.

[5] Z. Rahmati, M. Roushani, H. Hosseini, H. Choobin, Electrochemical immunosensor with Cu_2O nanocube coating for detection of SARS-CoV-2 spike protein, Biosens. Bioelectron. 188 (3) (2021), 105, https://doi.org/10.1007/s00604-021-04762-9.

[6] H. Zhang, B. Li, H. Chuan, Y. Liu, P. Xie, Immunoassay technology: Research progress in microcystin-LR detection in water samples, J. Hazard. Mater. 424 (2021), 127406, https://doi.org/10.1016/j.jhazmat.2021.127406.

[7] Z. Huang, X. Zhao, J. Hu, C. Zhang, X. Xie, R. Liu, Y. Lv, Single-Nanoparticle Differential Immunoassay for Multiplexed Gastric Cancer Biomarker Monitoring, Anal. Chem. 94 (37) (2022) 12899–12906, https://doi.org/10.1021/acs.analchem.2c03013.

[8] J. Kudr, P. Michalek, L. Ilieva, V. Adam, O. Zitka, COVID-19: A challenge for electrochemical biosensors, Trends. Anal. Chem. 136 (2021) 116192, https://doi.org/10.1016/j.trac.2021.116192.

[9] J. Abrego-Martinez, M. Jafari, G. S. Chergui, D. Che, M. Siaj, Aptamer-based electrochemical biosensor for rapid detection of SARS-CoV-2: Nanoscale electrode-aptamer-SARS-CoV-2 imaging by photo-induced force microscopy, Biosens. Bioelectron. 195 (2022), 113595, https://doi.org/10.1016/j.bios.2021.113595.

[10] Z. Rahmati, M. Roushani, H. Hosseini, H. Choobin, Electrochemical immunosensor with Cu_2O nanocube coating for detection of SARS-CoV-2 spike protein, Mikrochim Acta 188 (3) (2021) 105, https://doi.org/10.1007/s00604-021-04762-9.

[11] G. Mao, Y. Li, G. Wu, S. Ye, S. Cao, W. Zhao, J. Lu, J. Dai, Y. Ma, Construction of ratiometric Si-Mn:ZnSe nanoparticles for the immunoassay of SARS-CoV-2 spike protein, Sensor. Actuat. B-Chem. 369 (2022), 132306, https://doi.org/10.1016/j.snb.2022.132306.

[12] Y. Li, D. Lai, Q. Lei, Z. Xu, F. Wang, H. Hou, L. Chen, J. Wu, Y. Ren, M. Ma, B. Zhang, H. Chen, C. Yu, J. Xue, Y. Zheng, X. Wang, H. Jiang, H. Zhang, H. Qi, S. Guo, Y. Zhang, X. Lin, Z. Yao, P. Pang, D. Shi, W. Wang, X. Yang, J. Zhou, H. Sheng, Z. Sun, H. Shan, X. Fan, S. Tao, Systematic evaluation of IgG responses to SARS-CoV-2 spike protein-derived peptides for monitoring COVID-19 patients, Cell Mol. Immunol. 18 (3) (2021) 621–631, https://doi.org/10.1038/s41423-020-00612-5.

[13] M. Mehmandoust, Z.P. Gumus, M. Soylak, N. Erk, Electrochemical immunosensor for rapid and highly sensitive detection of SARS-CoV-2 antigen in the nasal sample, Talanta 240 (2022), 123211, https://doi.org/10.1016/j.talanta.2022.123211.

[14] Z. Rahmati, M. Roushani, SARS-CoV-2 virus label-free electrochemical nanohybrid MIP-aptasensor based on $Ni_3(BTC)_2$ MOF as a high-performance surface substrate, Mikrochim Acta 189 (8) (2022) 287, https://doi.org/10.1007/s00604-022-05357-8.

[15] T. Wu, H. Huang, Y. Sheng, H. Shi, Y. Min, Y. Liu, Transglutaminase mediated PEGylation of nanobodies for targeted nano-drug delivery, J. Mater. Chem. B 6 (7) (2018) 1011–1017, https://doi.org/10.1039/C7TB03132G.

[16] D. Rao, K. Mei, T. Yan, Y. Wang, W. Wu, Y. Chen, J. Wang, Q. Zhang, S. Wu, Nanomechanical sensor for rapid and ultrasensitive detection of tumor markers in serum using nanobody, Nano Res. 15 (2) (2021) 1003–1012, https://doi.org/10.1007/s12274-021-3588-4.

[17] D. Schumacher, J. Helma, A.F.L. Schneider, H. Leonhardt, C.P.R. Hackenberger, Nanobodies: chemical functionalization strategies and intracellular applications, Angew. Chem. Int. Ed. 57 (9) (2018) 2314–2333, https://doi.org/10.1002/anie.201708459.

[18] M. Amouzadeh Tabrizi, L. Nazari, P. Acedo, A photo-electrochemical aptasensor for the determination of severe acute respiratory syndrome coronavirus 2 receptor-binding domain by using graphitic carbon nitride-cadmium sulfide quantum dots nanocomposite, Sens. Actuat. B-Chem. 345 (2021), 130377, https://doi.org/10.1016/j.snb.2021.130377.

[19] X. Ding, Z. Li, C. Liu, Monolithic, 3D-printed lab-on-disc platform for multiplexed molecular detection of SARS-CoV-2, Sens. Actuat. B-Chem. 351 (2022), 130998, https://doi.org/10.1016/j.snb.2021.130998.

[20] W. Zhao, J. Xu, H. Chen, Photoelectrochemical immunoassays, Anal. Chem. 90 (1) (2018) 615–627, https://doi.org/10.1021/acs.analchem.7b04672.

[21] Y. Zhou, H. Yin, S. Ai, Applications of two-dimensional layered nanomaterials in photoelectrochemical sensors: a comprehensive review, Coord. Chem. Rev. 447 (2021), 214156, https://doi.org/10.1016/j.ccr.2021.214156.

[22] J. Dong, F. Chen, L. Xu, P. Yan, J. Qian, Y. Chen, M. Yang, H. Li, Fabrication of sensitive photoelectrochemical aptasensor using Ag nanoparticles sensitized bismuth oxyiodide for determination of chloramphenicol, Microchem. J. 178 (2022), 107317, https://doi.org/10.1016/j.microc.2022.107317.

[23] Y. Li, M. Gu, X. Zhang, J. Fan, K. Lv, S.A.C. Carabineiro, F. Dong, 2D g-C_3N_4 for advancement of photo-generated carrier dynamics: status and challenges, Mater. Today 41 (2020) 270–303, https://doi.org/10.1016/j.mattod.2020.09.004.

[24] M. Aggarwal, S. Basu, N.P. Shetti, M.N. Nadagouda, E.E. Kwon, Y.-K. Park, T. M. Aminabhavi, Photocatalytic carbon dioxide reduction: Exploring the role of ultrathin 2D graphitic carbon nitride (g-C_3N_4), Chem. Eng. J. 425 (2021), 131402, https://doi.org/10.1016/j.cej.2021.131402.

[25] M. Yang, Y. Jia, Y. Chen, P. Yan, L. Xu, J. Qian, F. Chen, H. Li, Fabrication of a photoelectrochemical aptasensor for sensitively detecting enrofloxacin antibiotic based on g-C_3N_4/$Bi_{24}O_{31}Cl_{10}$ heterojunction, J. Environ. Chem. Eng. 10 (2) (2022), 106208, https://doi.org/10.1016/j.jece.2022.107208.

[26] Y. Chen, L. Xu, M. Yang, Y. Jia, Y. Yan, J. Qian, F. Chen, H. Li, Design of 2D/2D CoAl LDH/ g-C_3N_4 heterojunction-driven signal amplification: fabrication and assay for photoelectrochemical aptasensor of ofloxacin, Sens. Actuators B-Chem. 353 (2022), 135187, https://doi.org/10.1016/j.snb.2021.131187.

[27] Y. Chen, M. Yang, Y. Jia, P. Yan, F. Chen, J. Qian, L. Xu, H. Li, NiS_2/NiFe LDH// g-C_3N_4 ternary heterostructure-based label-free photoelectrochemical aptasensing

for highly sensitive determination of enrofloxacin, Mater. Today Chem. 24 (2022), 100845, https://doi.org/10.1016/j.mtchem.2022.100845.
[28] C. Chu, N. Li, T. Xu, F. Gao, C. Qi, W. Lu, W. Chen, Polymeric iron phthalocyanine//g-C_3N_4 composite catalyst by mechanical force enhanced stripping and recombination for solar-induced contaminant degradation and CO_2 reduction, Appl. Surf. Sci. 592 (2022), 153308, https://doi.org/10.1016/j.apsusc.2022.153308.
[29] C. Li, X. Dong, Y. Zhang, J. Hu, J. Yuan, G. Li, D. Chen, Y. Li, Micro-tailored g-C_3N_4 enables Ru single-atom loading for efficient photocatalytic H_2 evolution, Appl. Surf. Sci. 596 (2022), 153471, https://doi.org/10.1016/j.apsusc.2022.153471.
[30] H. Liu, X. Li, Z. Ma, M. Sun, M. Li, Z. Zhang, L. Zhang, Z. Tang, Y. Yao, B. Huang, S. Guo, Atomically dispersed Cu catalyst for efficient chemoselective hydrogenation reaction, Nano Lett. 21 (24) (2021) 10284–10291, https://doi.org/10.1021/acs.nanolett.1c03381.
[31] J. Kroger, F. Podjaski, G. Savasci, I. Moudrakovski, A. Jimenez-Solano, M. W. Terban, S. Bette, V. Duppel, M. Joos, A. Senocrate, R. Dinnebier, C. Ochsenfeld, B.V. Lotsch, Conductivity mechanism in ionic 2D carbon nitrides: from hydrated ion motion to enhanced photocatalysis, Adv. Mater. 34 (7) (2021) 2107061, https://doi.org/10.1002/adma.202107061.
[32] L. Xu, W. Duan, F. Chen, J. Zhang, H. Li, A photoelectrochemical aptasensor for the determination of bisphenol A based on the Cu (I) modified graphitic carbon nitride, J. Hazard. Mater. 400 (2020), 123162, https://doi.org/10.1016/j.jhazmat.2020.123162.
[33] Y. Qin, J. Wen, L. Zheng, H. Yan, L. Jiao, X. Wang, X. Cai, Y. Wu, G. Chen, L. Chen, L. Hu, W. Gu, C. Zhu, Single-atom-based Heterojunction coupling with ion-exchange reaction for sensitive photoelectrochemical immunoassay, Nano Lett. 21 (4) (2021) 1879–1887, https://doi.org/10.1021/acs.nanolett.1c00076.
[34] B. Li, L. Guo, M. Chen, Y. Guo, L. Ge, H.F. Kwok, Single-atom Pt-anchored $Zn_{0.5}Cd_{0.5}S$ boosted photoelectrochemical immunoassay of prostate-specific antigen, Biosens. Bioelectron. 202 (2022), 114006, https://doi.org/10.1016/j.bios.2022.114006.
[35] H. Zhang, J. Wang, H. Duan, J. Ren, H. Zhao, C. Zhou, J. Qi, Mn^{3+} partially substituting the Ni^{3+} of $NiCo_2O_4$ enhance the charge transfer kinetics and reaction activity for hybrid supercapacitor, Appl. Surf. Sci. 597 (2022), 153617, https://doi.org/10.1016/j.apsusc.2022.153617.
[36] J. Gai, L. Ma, G. Li, M. Zhu, P. Qiao, X. Li, H. Zhang, Y. Zhang, Y. Chen, W. Ji, H. Zhang, H. Cao, X. Li, R. Gong, Y. Wan, A potent neutralizing nanobody against SARS-CoV-2 with inhaled delivery potential, Med. Comm. 2 (1) (2021) 101–113, https://doi.org/10.1002/mco2.60.
[37] I. Krivtsov, D. Mitoraj, C. Adler, M. Ilkaeva, M. Sardo, L. Mafra, C. Neumann, A. Turchanin, C. Li, B. Dietzek, R. Leiter, J. Biskupek, U. Kaiser, C. Im, B. Kirchhoff, T. Jacob, R. Beranek, Water-soluble polymeric carbon nitride colloidal nanoparticles for highly selective quasi-homogeneous photocatalysis, Angew. Chem. Int. Ed. 59 (1) (2020) 487–495, https://doi.org/10.1002/anie.201913331.
[38] H. Li, D. Wang, C. Miao, F. xia, Y. Wang, Y. Wang, C. Liu, G. Che, g-C_3N_4/BiOI S-scheme heterojunction: a 2D/2D model platform for visible-light-driven photocatalytic CO_2 reduction and pollutant degradation, J. Environ. Chem. Eng. (2022), 108201, https://doi.org/10.1016/j.jece.2022.108201.
[39] W. Wang, H. Zhang, S. Zhang, Y. Liu, G. Wang, C. Sun, H. Zhao, Potassium-ion-assisted regeneration of active cyano groups in carbon nitride nanoribbons: visible-light-driven photocatalytic nitrogen reduction, Angew. Chem. Int. Ed. 58 (46) (2019) 16644–16650, https://doi.org/10.1002/anie.201908640.
[40] W. Duan, P. Yan, J. Dong, Y. Chen, X. He, J. Chen, J. Qian, L. Xu, H. Li, A self-powered photoelectrochemical aptamer probe for oxytetracycline based on the use of a NiO nanocrystal/g-C_3N_4 heterojunction, Mikrochim. Acta 186 (11) (2019) 737, https://doi.org/10.1007/s00604-019-3856-0.
[41] Y. Hu, Y. Qu, Y. Zhou, Z. Wang, H. Wang, B. Yang, Z. Yu, Y. Wu, Single Pt atom-anchored C_3N_4: A bridging Pt–N bond boosted electron transfer for highly efficient photocatalytic H_2 generation, Chem. Eng. J. 412 (2021), 128749, https://doi.org/10.1016/j.cej.2021.128749.
[42] J. Tian, L. Zhang, M. Wang, X. Jin, Y. Zhou, J. Liu, J. Shi, Remarkably enhanced H_2 evolution activity of oxidized graphitic carbon nitride by an extremely facile K_2CO_3-activation approach, Appl. Catal. B 232 (2018) 322–329, https://doi.org/10.1016/j.apcatb.2018.03.076.
[43] Z. Zhang, W. Liu, Y. Zhang, J. Bai, J. Liu, Bioinspired atomic manganese site accelerates oxo-dehydrogenation of N-heterocycles over a conjugated tri-s-triazine framework, ACS Catal. 11 (1) (2020) 313–322, https://doi.org/10.1021/acscatal.0c04651.
[44] Z. Guo, Y. Xie, J. Xiao, Z. Zhao, Y. Wang, Z. Xu, Y. Zhang, L. Yin, H. Cao, J. Gong, Single-atom Mn-N_4 site-catalyzed peroxone reaction for the efficient production of hydroxyl radicals in an acidic solution, J. Am. Chem. Soc. 141 (30) (2019) 12005–12010, https://doi.org/10.1021/jacs.9b04569.
[45] Z. Chen, S. Mitchell, E. Vorobyeva, R.K. Leary, R. Hauert, T. Furnival, Q. M. Ramasse, J.M. Thomas, P.A. Midgley, D. Dontsova, M. Antonietti, S. Pogodin, N. López, J. Pérez-Ramírez, Stabilization of single metal atoms on graphitic carbon nitride, Adv. Funct. Mater. 27 (8) (2017) 1605785, https://doi.org/10.1002/adfm.201605785.
[46] J. Feng, H. Gao, L. Zheng, Z. Chen, S. Zeng, C. Jiang, H. Dong, L. Liu, S. Zhang, X. Zhang, A Mn-N_3 single-atom catalyst embedded in graphitic carbon nitride for efficient CO_2 electroreduction, Nat. Commun. 11 (1) (2020) 4341, https://doi.org/10.1038/s41467-020-18143-y.
[47] H. Fang, H. Guo, C. Niu, C. Liang, D. Huang, N. Tang, H. Liu, Y. Yang, L. Li, Hollow tubular graphitic carbon nitride catalyst with adjustable nitrogen vacancy: Enhanced optical absorption and carrier separation for improving photocatalytic activity, Chem. Eng. J. 402 (2020), 126185, https://doi.org/10.1016/j.cej.2020.126185.
[48] S.M. Yakout, New efficient sunlight photocatalysts based on Gd, Nb, V and Mn doped alpha-Bi_2O_3 phase, J. Environ. Chem. Eng. 8 (2020), 103644, https://doi.org/10.1016/j.jece.2019.103644.
[49] C. He, W. Xia, C. Zhou, D. Huang, C. Zhang, B. Song, Y. Yang, J. Li, X. Xu, Y. Shang, L. Du, Rational design to manganese and oxygen co-doped polymeric carbon nitride for efficient nonradical activation of peroxymonosulfate and the mechanism insight, Chem. Eng. J. 430 (2022), 132751, https://doi.org/10.1016/j.cej.2021.132751.
[50] P. Yan, Z. Mo, J. Dong, F. Chen, J. Qian, J. Xia, L. Xu, J. Zhang, H. Li, Construction of Mn valence-engineered MnO_2/BiOCl heterojunction coupled with carriers-trapping effect for enhanced photoelectrochemical lincomycin aptasensor, Sens. Actuators B-Chem. 320 (2020), 128415, https://doi.org/10.1016/j.snb.2020.128415.
[51] F. Rahbarizadeh, D. Ahmadvand, Z. Sharifzadeh, Nanobody; an old concept and new vehicle for immunotargeting, Immunol. Invest 40 (3) (2011) 299–338, https://doi.org/10.3109/08820139.2010.542228.
[52] M. Dumoulin, K. Conrath, A. Van Meirhaeghe, F. Meersman, K. Heremans, L. G. Frenken, S. Muyldermans, L. Wyns, A. Matagne, Single-domain antibody fragments with high conformational stability, Protein Sci. 11 (3) (2002) 500–515, https://doi.org/10.1110/ps.34602.